JAST, Vol. 6, No. 1, pp 13–23

JAST
Journal of Aerospace Science and Technology

A Fast Mesh-Free Galerkin Method for the Analysis of Steady-State Heat Transfer

S. Forouzan-Sepehr[1], S. Mohammadi[2]

The element-free Galerkin method is employed for a two-dimensional analysis of steady-state heat transfer. The unknown response of the system, i.e. temperature, is approximated using the moving least squares technique. Numerical integration of governing simultaneous system of equations is performed by Gauss quadrature and new modified nodal integration techniques. Numerical examples and tests have proved that the new methods remain in an acceptable level of accuracy while providing less expensive and much faster approaches.

INTRODUCTION

The finite element (FE) method, though vastly used in analysis of engineering problems, has some evident limitations. It requires an appropriate initial mesh to obtain proper results. Values of derivatives of the field parameter or system response (*e.g.* temperature in this study) have a lower order of smoothness and accuracy due to local interpolation nature of the analysis, and finally the data transfer procedure from an old to a new mesh in an adaptive analysis is a time-consuming and expensive task.

To overcome the above mentioned limitations, several mesh-free methods have been proposed by researchers. The smoothed particle hydrodynamics (SPH) [1], the element-free Galerkin (EFG) method [2-5], the meshless local Petrov-Galerkin (MLPG) method [6], and the reproducing kernel particle method (RKPM) [7] are among many available mesh-free approaches. The EFG method, among others, has less complexity and more efficiency, and has been successfully employed to solve several engineering problems such as analysis of plates and shells [8-9], wave propagation [10], contact mechanics [11], and heat transfer [12-17], etc. An obvious disadvantage of nearly all mesh-free methods is in their requirement for far more CPU time than their FE counterparts, since:

1. Mesh-free shape functions and their derivatives cannot be derived in closed form formulations, and are computationally more complex than the well-developed FE shape functions.
2. Far more Gauss points are required for Gauss quadrature integration in mesh-free methods than in the FE method.

In this article, several numerical integration techniques have been developed and implemented within the EFG method together with Lagrange multipliers (to enforce the essential boundary conditions) for two-dimensional analysis of steady-state heat transfer.

Several examples simulated by object-oriented software is specifically developed for this purpose. Numerical examples have been used to assess the performance of the method, and to evaluate the quality and accuracy of the proposed nodal integration techniques.

PARTIAL DIFFERENTIAL EQUATION OF HEAT TRANSFER AND DISCRETISATION

Quasi-harmonic partial differential equations, generally expressed as:

$$\nabla^T \mathbf{k} \nabla T + Q_0 - \alpha_0 T - \beta_0 \frac{\partial T}{\partial t} - \gamma_0 \frac{\partial^2 T}{\partial t^2} = 0 \qquad (1)$$

in a domain Ω, cover a wide range of engineering problems depending on the definition of parameters included in Eq. (1), and therefore can be classified into four categories:

1. General quasi-harmonic PDE: where $\beta_0 \neq 0$ and $\gamma_0 \neq 0$, such as in fluid mechanics and damped wave motions.
2. Helmholtz wave equation: in the case of $\beta_0 = 0$ and $\gamma_0 \neq 0$, such as electromagnetic waves, fluid surface

1. *Ph.D. Candidate, School of Civil Eng., Univ. of Tehran, Tehran, Iran.*
2. *Associate Professor, School of Civil Eng., Univ. of Tehran, Tehran, Iran, Email:smoham@ut.ac.ir.*

waves and compression waves, the general quasi-harmonic equation yields to a hyperbolic PDE.

3. Transient heat conduction equation: transient heat conduction, soil consolidation and any other diffusion process can be modelled by a parabolic PDE, *i.e.*, the case for $\beta_0 \neq 0$ and $\gamma_0 = 0$.
4. Steady-state heat transfer equation: an elliptic PDE ($\beta_0 = 0$ and $\gamma_0 = 0$ condition) which can be used to model steady-state heat transfer, seepage, irrotational flow of ideal fluids, distribution of electrical or magnetic potential, torsion of prismatic shaft, *etc.* is used in this study with proper boundary conditions.

On the other hand, the governing equations for a steady-state heat transfer in a system with domain Ω and boundary Γ (Figure 1) are considered as:

$$\begin{cases} \nabla^T \mathbf{k} \nabla T + h\left(T_{\text{ext}} - T\right) + Q = 0 & ; \text{in}\,\Omega \\ \left(\mathbf{k}\nabla T\right)^T \mathbf{n} - \bar{q} - \alpha T = 0 & ; \text{on}\,\Gamma_q \\ T = \bar{T} & ; \text{on}\,\Gamma_T \end{cases} \tag{2}$$

where T, T^{ex} and $\bar{T}$ are temperature, its exact value and specified boundary temperature, respectively, with $\mathbf{n}$ as the unit vector normal to the boundary. $\mathbf{k} = diag[k_x\ k_y]$ defines the matrix of conductivity in terms of its x and y coefficients. h and α are the conductive heat transfer and radiation coefficients, respectively. Q is the heat source (rate of heat transfer per unit volume) and $\bar{q}$ is the specified heat flux on the boundary (rate of heat transfer per unit area). Eq. (2) can be implemented in a weak form as:

$$\begin{aligned} \Pi(T,\lambda) = \frac{1}{2}\int_{\Omega} (\nabla T)^T \mathbf{k}\,(\nabla T)\,d\Omega - \int_{\Omega} (hT_{\text{ext}} + Q)\,T d\Omega \\ + \frac{1}{2}\int_{\Omega} hT^2 d\Omega + \frac{1}{2}\int_{\Gamma_q} \alpha T^2 d\Gamma + \int_{\Gamma_q} \bar{q} T d\Gamma \\ + \int_{\Gamma_T} \lambda\left(T - \bar{T}\right) d\Gamma \end{aligned} \tag{3}$$

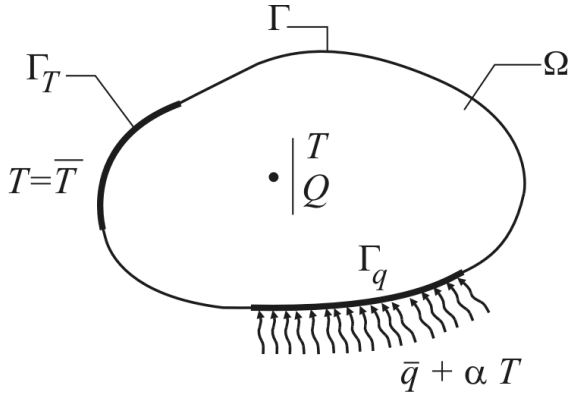

Figure 1. Typical steady-state heat transfer problem.

where λ is the Lagrange multiplier function. After substituting:

$$T(\mathbf{x}) \cong T^{\text{h}}(\mathbf{x}) = \mathbf{\Phi}(\mathbf{x})\,\mathbf{a} \tag{4}$$

$$\lambda(\mathbf{x}) = \mathbf{N}_{\lambda}(\mathbf{x})\,\lambda \tag{5}$$

where Φ is the matrix of MLS shape functions, N_λ is the Lagrange interpolation matrix, and T^h is the numerical approximation of temperature. Eq. (3) is minimised with respect to the unknowns $\mathbf{a}$ (vector of nodal temperatures) and λ:

$$\frac{\partial \Pi(\mathbf{a},\lambda)}{\partial(\mathbf{a},\lambda)} = \mathbf{0} \tag{6}$$

which yields a simultaneous system of equations:

$$\begin{bmatrix} \mathbf{K} & \mathbf{G} \\ \mathbf{G}^{\text{T}} & \mathbf{0} \end{bmatrix} \begin{Bmatrix} \mathbf{a} \\ \lambda \end{Bmatrix} = \begin{Bmatrix} \mathbf{f} \\ \mathbf{f}_{\lambda} \end{Bmatrix} \tag{7}$$

The stiffness matrix $\mathbf{K}$ and the vector of nodal forces $\mathbf{f}$ are obtained from:

$$\mathbf{K} = \mathbf{K}_k + \mathbf{K}_h + \mathbf{K}_{\alpha} \tag{8}$$

$$\mathbf{f} = \mathbf{f}_h + \mathbf{f}_Q + \mathbf{f}_{\bar{q}} \tag{9}$$

where matrices $\mathbf{K}_k$, $\mathbf{K}_h$ and $\mathbf{K}_\alpha$ are related to conduction, convection and radiation, respectively, and can be calculated from:

$$\mathbf{K}_k = \int_{\Omega} (\nabla \mathbf{\Phi})^T \mathbf{k}\,(\nabla \mathbf{\Phi})\,d\Omega \tag{10}$$

$$\mathbf{K}_h = \int_{\Omega} h \mathbf{\Phi}^{\text{T}} \mathbf{\Phi} d\Omega \tag{11}$$

$$\mathbf{K}_{\alpha} = \int_{\Gamma_q} \alpha \mathbf{\Phi}^{\text{T}} \mathbf{\Phi} d\Gamma \tag{12}$$

Nodal force vectors $\mathbf{f}_h$, $\mathbf{f}_Q$ and $\mathbf{f}_q$, associated to convection, heat source and boundary heat flux, respectively, are defined as:

$$\mathbf{f}_h = \int_{\Omega} h T_{\text{ext}} \mathbf{\Phi}^{\text{T}} d\Omega \tag{13}$$

$$\mathbf{f}_Q = \int_{\Omega} Q \mathbf{\Phi}^{\text{T}} d\Omega \tag{14}$$

$$\mathbf{f}_{\bar{q}} = \int_{\Gamma_q} \bar{q} \mathbf{\Phi}^{\text{T}} d\Gamma \tag{15}$$

Matrix $\mathbf{G}$ and vector $\mathbf{f}_\lambda$ are related to the Lagrange multiplier $\lambda(\mathbf{x})$ and can be defined as:

$$\mathbf{G} = \int_{\Gamma_T} \mathbf{\Phi}^{\mathrm{T}} \mathbf{N}_\lambda d\Gamma \tag{16}$$

$$\mathbf{f}_\lambda = \int_{\Gamma_T} \bar{T} \mathbf{N}_\lambda^{\mathrm{T}} d\Gamma \tag{17}$$

The EFG (MLS) shape function matrix $\mathbf{\Phi}(\mathbf{x})$ will be discussed in the next section. $\mathbf{N}_\lambda(\mathbf{x})$ is the matrix of Lagrange interpolation functions with the Kroneker delta property:

$$N_{\lambda_I}(\mathbf{x}_J) = \delta_{IJ} \tag{18}$$

Two types of strong and weak form error norms are adopted to evaluate the results of the proposed approaches:

$$e_T(\mathbf{x}) = \frac{\left|T^{\mathrm{ex}}(\mathbf{x}) - T^{\mathrm{h}}(\mathbf{x})\right|}{\left|T^{\mathrm{ex}}(\mathbf{x})\right|} \tag{19}$$

$$err(T) = \sqrt{\frac{\int_\Omega \left|T^{\mathrm{ex}}(\mathbf{x}) - T^{\mathrm{h}}(\mathbf{x})\right|^2 d\Omega}{\int_\Omega \left|T^{\mathrm{ex}}(\mathbf{x})\right|^2 d\Omega}} \tag{20}$$

$e_{T,x}(\mathbf{x})$ and $err(T_{,x})$ are defined similarly.

THE ELEMENT-FREE GALERKIN METHOD

Belytschko *et.al.* [2] introduced the element-free Galerkin (EFG) method in 1994 based on the concepts of the moving least squares (MLS) approximation with the following properties:

- By using MLS approximation instead of interpolation, smoother and more continuous results can be obtained [16].
- MLS is a local approximation, and as such, is more accurate than the global least squares [16].

Moving Least Squares Approximation

Lancaster *et.al.* [17] expanded the least squares global curve fitting to the local moving least squares approximation. In this method, the field parameter value (here, temperature) at any point of the system domain Ω can be approximated by:

$$T(\mathbf{x}) \cong T^{\mathrm{h}}(\mathbf{x}) = \mathbf{p}^{\mathrm{T}}(\mathbf{x})\,\alpha(\mathbf{x}) \tag{21}$$

where $\mathbf{p}(\mathbf{x})$ is the vector of m basis functions,

$$\mathbf{p}(\mathbf{x}) = \left[1\,,\ x\,,\ y\,,\ x^2\,,\ xy\,,\ y^2\,,\ \ldots\right]^{\mathrm{T}}_{1\times m} \tag{22}$$

and $\alpha(\mathbf{x})$ is the vector of unknown multipliers as a function of $\mathbf{x}$. If the values of the temperatures are described at N nodes $\mathbf{x}_1, \mathbf{x}_2, \ldots, \mathbf{x}_N$ as a vector such as:

$$\mathbf{a} = \left[T_1\,,\ T_2\,,\ \ldots\,,\ T_N\right]^{\mathrm{T}}_{1\times N} \tag{23}$$

where $T_I = T(\mathbf{x}_I)$; $I = \overline{1, N}$, Eq. (21) can be rewritten as:

$$T^{\mathrm{h}}(\mathbf{x}, \mathbf{x}_I) = \mathbf{p}^{\mathrm{T}}(\mathbf{x}_I)\,\alpha(\mathbf{x}) \qquad ; \quad I = \overline{1, N} \tag{24}$$

to locally approximate the field parameter, the unknown vector $\alpha(\mathbf{x})$ can then be obtained by minimising the following L_2 norm:

$$\begin{aligned} J(\mathbf{x}) &= \tfrac{1}{2}\sum_{I=1}^{N} w(\mathbf{x} - \mathbf{x}_I)\left(T^{\mathrm{h}}(\mathbf{x}, \mathbf{x}_I) - T_I\right)^2 \\ &= \tfrac{1}{2}\left(\mathbf{P}\alpha(\mathbf{x}) - \mathbf{a}\right)^{\mathrm{T}} \mathbf{W}(\mathbf{x})\left(\mathbf{P}\alpha(\mathbf{x}) - \mathbf{a}\right) \end{aligned} \tag{25}$$

where the matrices $\mathbf{P}_{N\times m}$ and $\mathbf{W}_{N\times N}(\mathbf{x})$ are defined as:

$$P_{Ij} = p_j(\mathbf{x}_I) \qquad ; \quad I = \overline{1, N}\ \&\ j = \overline{1, m} \tag{26}$$

$$\mathbf{W}(\mathbf{x}) = \underset{I=\overline{1,N}}{\mathrm{diag}}\left[w(\mathbf{x} - \mathbf{x}_I)\right] \tag{27}$$

respectively. $w(x - x_I)$ is a predefined weight function, and will be explained in next section. Minimising $J(\mathbf{x})$ with respect to $\alpha(\mathbf{x})$:

$$\frac{\partial J(\mathbf{x})}{\partial \alpha(\mathbf{x})} = \mathbf{A}(\mathbf{x})\alpha(\mathbf{x}) - \mathbf{B}(\mathbf{x})\mathbf{a} = \mathbf{0} \tag{28}$$

where

$$\mathbf{A}(\mathbf{x}) = \mathbf{P}^{\mathrm{T}}\mathbf{W}(\mathbf{x})\mathbf{P} \tag{29}$$

$$\mathbf{B}(\mathbf{x}) = \mathbf{P}^{\mathrm{T}}\mathbf{W}(\mathbf{x}) \tag{30}$$

the vector of unknowns $\alpha(\mathbf{x})$ is obtained as:

$$\alpha(\mathbf{x}) = \mathbf{A}^{-1}(\mathbf{x})\mathbf{B}(\mathbf{x})\mathbf{a} \tag{31}$$

Substituting Eq. (31) into (21) and comparing it with Eq. (5) yields:

$$\mathbf{\Phi}(\mathbf{x}) = \mathbf{p}^{\mathrm{T}}(\mathbf{x})\mathbf{A}^{-1}(\mathbf{x})\mathbf{B}(\mathbf{x}) \tag{32}$$

The MLS shape functions do not possess the Kroneker delta property:

$$\Phi_I(\mathbf{x}_J) \neq \delta_{IJ} \tag{33}$$

They only provide an approximate solution, and should not be considered as interpolation functions. Nevertheless, they satisfy constant and linear consistency conditions:

$$\sum_{I=1}^{N} \Phi_I(\mathbf{x}_J) \cdot 1 = 1 \qquad ; \quad J = \overline{1,N} \tag{34}$$

$$\sum_{I=1}^{N} \Phi_I(\mathbf{x}_J) \cdot \mathbf{x}_I = \mathbf{x}_J \qquad ; \quad J = \overline{1,N} \tag{35}$$

The first derivative set of shape functions are employed to determine the conductive part of the stiffness matrix:

$$\mathbf{\Phi}_{,\mathbf{x}} = \partial \mathbf{\Phi}(\mathbf{x})/\partial \mathbf{x} = \mathbf{p}_{,\mathbf{x}}^{\mathrm{T}} \mathbf{A}^{-1} \mathbf{B} + \mathbf{p}^{\mathrm{T}} \mathbf{A}^{-1} \left(\mathbf{B}_{,\mathbf{x}} - \mathbf{A}_{,\mathbf{x}} \mathbf{A}^{-1} \mathbf{B} \right) \tag{36}$$

Weight Function

It can be stated that by introduction of the weight function w in Eq. (25), the MLS method generates a local robust approximation. The weight function $w(\mathbf{x} - \mathbf{x}_I)$ is a positive non-zero monotonic decreasing function in a special sub-domain Ω_I of the system called the influence domain associated with node $\mathbf{x}_I$:

$$w\left(\mathbf{x} - \mathbf{x}_I\right) = \begin{cases} w\left(\xi\right) > 0 & ; \quad x \in \Omega_I \\ 0 & ; \quad \text{otherwise} \end{cases} \tag{37}$$

where

$$\xi = \frac{\|\mathbf{x} - \mathbf{x}_I\|}{\rho_I} \tag{38}$$

It is necessary to define three different sets of sub-domains related to a system Ω (Figure 2):

1. Total Domain of Influence $\hat{\Omega}_I$ associated to any node I of the system:

$$\hat{\Omega}_I = \{\mathbf{x} : \|\mathbf{x} - \mathbf{x}_I\| < \rho_I\} \tag{39}$$

2. Exact Influence Domain Ω_I associated to any node I of the system:

$$\Omega_I = \{\mathbf{x} \in \Omega : \|\mathbf{x} - \mathbf{x}_I\| < \rho_I\} \tag{40}$$

3. Domain of Neighbourhood ω_x' associated to any point $\mathbf{x} \in \Omega$:

$$\Omega_{\mathbf{x}}' = \left\{\mathbf{x}_I \in \Omega : \|\mathbf{x} - \mathbf{x}_I\| < \rho_I \ , \ I = \overline{1,N}\right\} \tag{41}$$

It is evident that:

$$\Omega_I = \hat{\Omega}_I \cap \Omega \tag{42}$$

$$\Omega = \bigcup_{I=1}^{N} \Omega_I \tag{43}$$

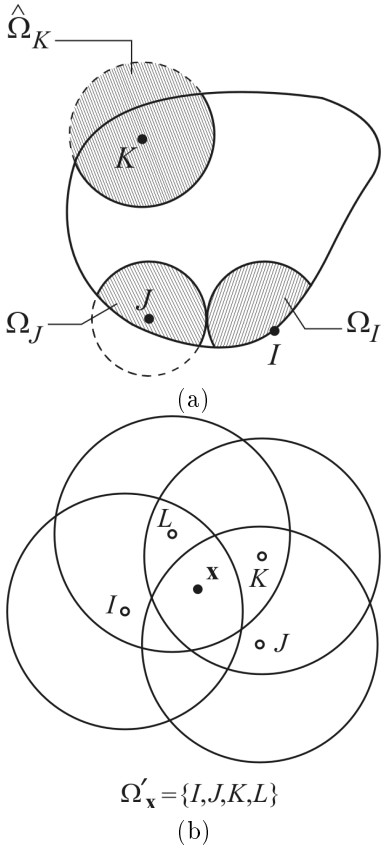

Figure 2. Typical sets of sub-domains: (a) total and exact influence domains (b) neighbourhood domain.

$$\Omega \subseteq \bigcup_{I=1}^{N} \hat{\Omega}_I \tag{44}$$

The MLS approximation is well defined if the matrix $\mathbf{A}(\mathbf{x})$ in Eq. (28) is non-singular. This is achieved where there are enough non-zero weight functions, or enough nodes, within the influence domain of each nodes of the system. Therefore, the domain of influence of each node:

1. Must be large enough to include enough nodes for $\mathbf{A}(\mathbf{x})$ to be non-zero, *i.e.*

$$N_I \geq m \tag{45}$$

2. Must be small enough to satisfy the locality behaviour of the MLS approximation.

To maintain the above conditions, $(\rho_{req})_I$ the minimum required value of the radius of influence domain of each node I is taken as $||\mathbf{x}_K - \mathbf{x}_I||$ where $\mathbf{x}_K$ is the m^{th} nearest node to node I regardless of the node itself. Its radius of influence domain ρ_I can then be defined as:

$$\rho_I = \max\left(\alpha_\rho \cdot (\rho_{\mathrm{req}})_I, \rho_{\min}\right) \tag{46}$$

The smoothness of MLS shape function $\mathbf{\Phi}(\mathbf{x})$ is determined by that of the basis functions and the weight

function. Let $C^k(\Omega)$ be the space of k^{th} continuously differentiable function. If $w(\zeta) \in C^k(\Omega)$ and $\mathbf{p}(\mathbf{x}) \in C^l(\Omega)$, then it can be shown that $\mathbf{\Phi}(\mathbf{x}) \in C^{\min(k,l)}(\Omega)$.

NUMERICAL INTEGRATION

Due to the complexity of the EFG shape functions, it is obviously impossible to determine the exact values of integrals constituting the stiffness matrix and the nodal force vector. Therefore, two categories of numerical integration techniques have been employed to approximate them:

- Gauss Quadrature Using Background Cells
- Nodal Integration

Condition of the assembled matrix $\mathbf{K}^* = \begin{bmatrix} \mathbf{K} & \mathbf{G} \\ \mathbf{G}^{\mathrm{T}} & \mathbf{0} \end{bmatrix}$ defined as:

$$\mathrm{cond}\left(\mathbf{K}^*\right) = \det\left(\mathbf{K}^*\right) \cdot \det\left(\mathbf{K}^{*^{-1}}\right) \tag{47}$$

and expected to be near 1.0, together with some patch tests are employed in this paper as means of evaluating the quality of integration.

Integration by Gauss Quadrature

In this technique, similar to FEM, Gauss points that are defined in a virtual mesh called background cell structure (Figure 3) are taken as the sampling points of the integration.

Therefore, integration of any given function $f(\mathbf{x})$ in the system domain Ω can be approximated by:

$$I(f) = \int_{\Omega} f(\mathbf{x}) d\Omega \approx \sum_{c} I_c \tag{48}$$

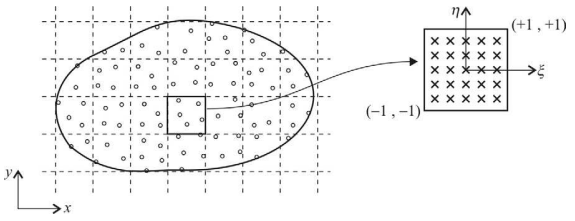

Figure 3. Integration by Gauss Quadrature.

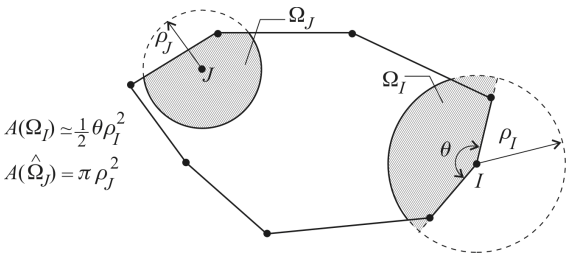

Figure 4. Definition of area A_I corresponding to any node I or J in the nodal integration approach 1.

$$\begin{aligned} I_c = \int_{\Omega_c} f(\mathbf{x}) d\Omega &= \int_{-1}^{+1}\int_{-1}^{+1} f_c(\xi,\eta) d\xi d\eta \\ &\approx \sum_{i=1}^{n_G}\sum_{j=1}^{n_G} q_{ij}^{\Omega_c} f_c\left(\xi_i, \eta_j\right) \end{aligned} \tag{49}$$

where $q_{ij}^{\Omega_c}$ is a weighting coefficient associated with the Gauss point $\mathbf{x}_{G_{ij}} = \begin{bmatrix} \xi_i & \eta_j \end{bmatrix}^{\mathrm{T}}$ within the cell c:

$$q_{ij}^{\Omega_c} = \tfrac{1}{4} w_i^{n_G} w_j^{n_G} A\left(\Omega_c\right) \tag{50}$$

In Eq. (50), $w_i^{n_G}$ and $w_j^{n_G}$ are weight coefficients of the n_G-point Gauss integration rule [18]. Numerical investigations indicate that while selection of the number of Gauss points and cells may affect the accuracy of results, increasing them does not necessarily increase the accuracy [16]. Some references (*e.g.* [2]) propose a background mesh of $n_c \times n_c$ cells, each containing $n_G \times n_G$ Gauss points:

$$n_c \approx \sqrt{N} \tag{51}$$

$$n_G \approx \sqrt{N}_c + 2 \tag{52}$$

where N_c represents the number of nodes within a cell. Nevertheless, it is evident that choosing a suitable background mesh and the number of Gauss points greatly depend on the order of basis and weight functions in addition to the nodal arrangement.

Because of locality of EFG shape functions and their derivatives, finding neighbourhood domain Ω'_{x_G} of each Gauss point $\mathbf{x}_G$, as an "initial processing" task, may speed up the main global assembly procedure.

Nodal Integration Methods

Numerical integration using the Gauss quadrature requires a background mesh comprising of Gauss points which are usually much more than the number of EFG nodes N. In order to develop a much faster approach, researchers have suggested employing only N nodes to evaluate the integrals [19-20]. Eqs. (48)-(49) can now be rewritten as:

$$I(f) = \int_{\Omega} f(\mathbf{x}) d\Omega \approx \sum_{I=1}^{N} \int_{\substack{\hat{\Omega}_I \\ \text{or} \\ \Omega_I}} \psi_{\mathrm{I}}(\mathbf{x}) f(\mathbf{x}) d\Omega \tag{53}$$

Duflot *et.al.* [19] proposed to let the integration weight function $\psi_I(\mathbf{x})$ be the Sheppard shape function, *i.e.*

$$\psi_I(\mathbf{x}) = \Phi_I^{\mathrm{Sheppard}}(\mathbf{x}) = \frac{w(\mathbf{x}-\mathbf{x}_I)}{\sum_{J=1}^{N} w(\mathbf{x}-\mathbf{x}_J)} \tag{54}$$

Though any function satisfying the partitions of unity condition can be employed as $\psi_I(\mathbf{x})$, defining the integration weight function as:

$$\psi_I(\mathbf{x}) = q_I^{\Omega} \cdot \delta\left(\mathbf{x}-\mathbf{x}_I\right) \tag{55}$$

simplifies Eq. (53) into:

$$I(f) \approx \sum_{I=1}^{N} q_I^{\Omega} f(\mathbf{x}_I) \tag{56}$$

where q_I^{Ω} is a portion of total area $A(\Omega)$ of the system associated with node I, which means that the quantities of $q_I^{\Omega}/A(\Omega)$ for $I = \overline{1, N}$ are partitions of unity:

$$\sum_{I=1}^{N} \frac{q_I^{\Omega}}{A(\Omega)} = 1 \tag{57}$$

On the other hand, Eq. (56) leads to an exact result when $f(\mathbf{x})$ is a constant function, a characteristic that integration by background cells does not generally possess.

Belytschko *et.al.* [20] proposed the following definitions for q_I^{Ω}:

$$q_I^{\Omega} = \frac{c_I \rho_I^2}{\sum_{J=1}^{N} c_J \rho_J^2} \cdot A(\Omega) \tag{58}$$

or

$$q_I^{\Omega} = \sum_{J=1}^{N} \int_{\Omega} \Phi_I(\mathbf{x}) \Phi_J(\mathbf{x}) d\Omega \tag{59}$$

where c_I is assumed to be 1.0 for all $\mathbf{x}_I \in \Omega - \Gamma$ and 0.25 or 0.5 for $\mathbf{x}_I \in \Gamma$ on a corner or elsewhere, respectively.

In the present study, q_I^{Ω} is simply defined as:

$$q_I^{\Omega} = \frac{A_I}{\sum_{J=1}^{N} A_J} \cdot A(\Omega) \tag{60}$$

where A_I is a predefined area corresponding to any node I. Three cases are investigated and compared with the Gauss quadrature integration:

1. **Approach 1:** Similar to the idea of Belytschko *et.al.* [20], A_I is defined as (Figure 4):

$$A_I = \begin{cases} A\left(\hat{\Omega}_I\right) = \pi \rho_I^2 & ; \quad \mathbf{x}_I \in \Omega - \Gamma \\ A(\Omega_I) \cong \frac{1}{2} \theta \rho_I^2 & ; \quad \mathbf{x}_I \in \Gamma \end{cases} \tag{61}$$

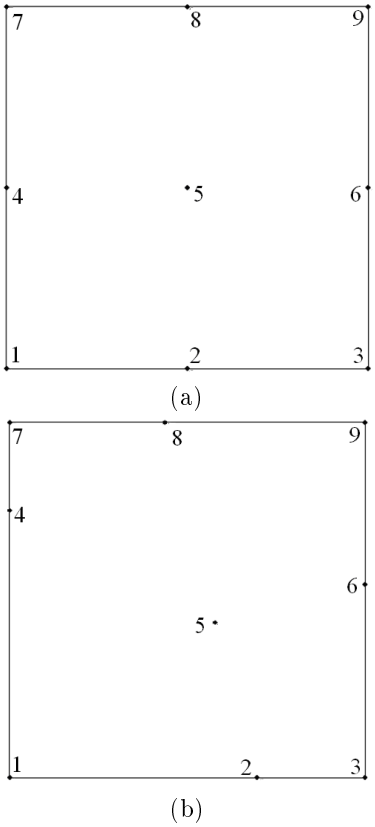

Figure 5. Nodal arrangements for the patch test: (a) regular arrangement (b) irregular arrangement.

2. **Approach 2**: Eq. (61) may generate a significant integration error for nodes inside the domain but very close to the boundary. Therefore, the exact area of the influence domain of a node can be used as an alternative to overcome this source of error:

$$A_I = A(\Omega_I) \tag{62}$$

3. **Approach 3:** In previous approaches, the area A_I depends only on the influence domain of node I, *i.e.* the number of influenced nodes required for a well-defined EFG shape function; while dependence of q_I^{Ω} on a proper portion of the whole system area and therefore, on nodal arrangement and distance between nodes seems to be more realistic and

Table 1. Results of the standard patch test.

Nodes Arrangement	Integration Technique	T_5^h	$e_T(\mathbf{x}_5)$	$\sum_{J=1}^{N} A_J \Big/ A(\Omega)$
Regular ($T_5^{ex} = 10.000$)	Gauss Quadrature	10.000	4.90E-12%	——
	Nodal Integ. Appr. 1	10.000	4.14E-11%	4.909
	Nodal Integ. Appr. 2	10.000	4.12E-11%	4.398
	Nodal Integ. Appr. 3	10.000	4.06E-11%	0.917
Irregular ($T_5^{ex} = 10.146$)	Gauss Quadrature	10.893	7.36%	——
	Nodal Integ. Appr. 1	11.167	10.06%	7.255
	Nodal Integ. Appr. 2	11.123	9.63%	5.874
	Nodal Integ. Appr. 3	10.909	7.52%	1.421

rational. Therefore, instead of taking A_I as the area of a circle or sector with the radius ρ_I, it is proposed in this study to take a new radius ρ'_I defined as one half of the average distance between the node I and its neighbours:

$$\rho'_I = \frac{1}{2} \cdot \frac{\sum_{J\,(\mathbf{x}_J \in \Omega_I)} \|\mathbf{x}_I - \mathbf{x}_J\|}{N_I} \tag{63}$$

Obviously, the value of $\sum_{J=1}^{N} A_J$ obtained in approach 3 is much closer to the system area $A(\Omega)$ than other approaches; therefore, better results are expected for the integrals.

Finding the influence domain Ω_I of each node I in nodal integration rules, as an "initial processing" procedure similar to the Gauss quadrature integration, may speed up generating the assembled matrix K^* and vector $f^* = [\mathbf{f}\ \mathbf{f}_\lambda]^T$ of the simultaneous system of equations.

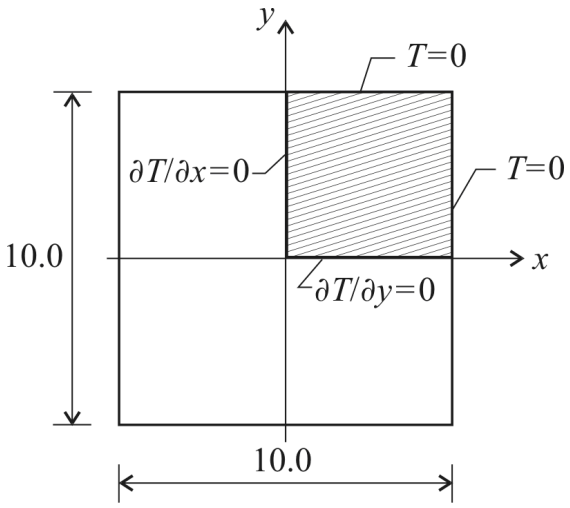

(a)

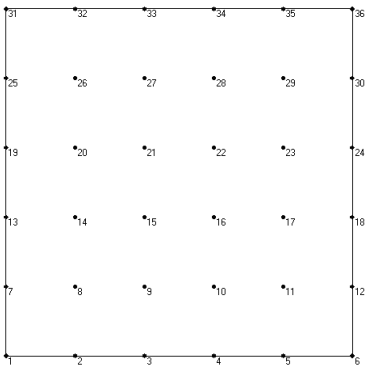

(b)

Figure 6. Analysis of the square fin: (a) geometry and boundary conditions (b) nodal arrangement.

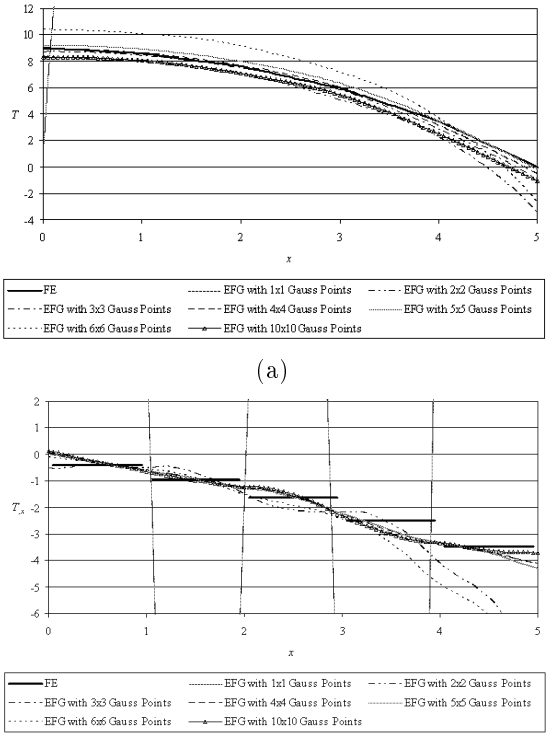

(a)

(b)

Figure 7. Analysis of the square fin at $y = 0$ using FE and EFG methods with different numbers of Gauss points: (a) temperature (b) first derivative of temperature.

NUMERICAL STUDIES

The proposed techniques of integration have been implemented within object-oriented software already developed for two-dimensional steady-state heat transfer analysis using the EFG method [21]. Several numerical examples are investigated to assess and compare the performance of the integration techniques.

A fourth order spline weight function is used for all numerical examples:

$$w(\xi) = \begin{cases} 1 - 6\xi^2 + 8\xi^3 - 3\xi^4 & ; \quad \xi < 1 \\ 0 & ; \quad \xi \geq 1 \end{cases} \tag{64}$$

Standard Patch Test

The standard patch test in a square domain of dimension 10.0×10.0, as shown in Figure 5, is considered in two cases: (a) regular nodal arrangement and (b) irregular nodal arrangement with the exact solution $T^{\text{ex}}(x, y) = x + y$.

Satisfaction of the patch test requires that the value of T^h at any interior node be equal to T^{ex}. Since, the exact solution is a linear function, a linear basis function vector ($m = 3$) is employed in the analysis. Gauss quadrature integration is performed using a cell which includes 3×3 Gauss points and 2 Gauss points on any boundary segments. All three nodal integration approaches are investigated. The scaling factor α_ρ

and the minimum radius of influence domain ρ_{min} are taken to be 1.25 and 5.0 for case (a) and 1.5 and 7.0 for case (b), respectively. Computational results illustrated in Table 1 show the EFG method using nodal integration techniques passes the standard patch test with an acceptable level of accuracy.

Square Fin

A square fin of dimension 10.0×10.0 which generates heat internally at a prescribed constant rate ($Q = 2.4$) and has zero temperature on the exterior boundaries, is considered as shown in Figure 6. The thermal conductive coefficients are assumed to be 2.0 in both the x and y directions and the radiation coefficient is taken to be 1.0. No convection takes place in this example. Because of the symmetry, only one quarter of the domain is modelled (Figure 6).

The scaling factor α_ρ and the minimum radius of influence domain ρ_{min} are taken to be 1.5 and 1.25, respectively. Quadratic basis ($m = 6$) is employed in the analysis. Gauss quadrature integration is performed using 5×5 cells, each including $n_G \times n_G$ Gauss points and 2 Gauss points on any boundary segments. Results illustrated in Figures 7-8 and Table 2 show the best accuracy is achieved for $N_G = 4$. Figure 7 depicts the analysis results for both the temperature and its first derivative at $y = 0$ using FE and EFG methods with different numbers of Gauss points. In Figure 8, the relative error at $y = 0$ was compared for different numbers of Gauss points. Figure 9 compares results of temperature value and its derivative at section $y = 0$ using EFG with different types of integration rules and FE. Relative errors and the time required to assemble the matrix $\mathbf{K}^*$ and the vector $\mathbf{f}^*$ are illustrated in Table 3. According to Table 3, the assembling CPU time with nodal integration rules is just about 5 percent of the CPU time required by Gauss quadrature integration, though nodal integration techniques have lower yet acceptable levels of accuracy.

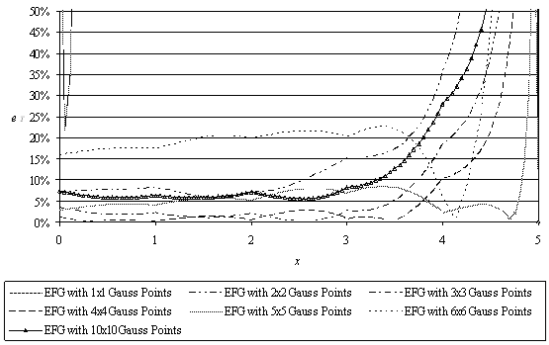

Figure 8. Relative error at $y = 0$ of the square fin comparing different numbers of Gauss points.

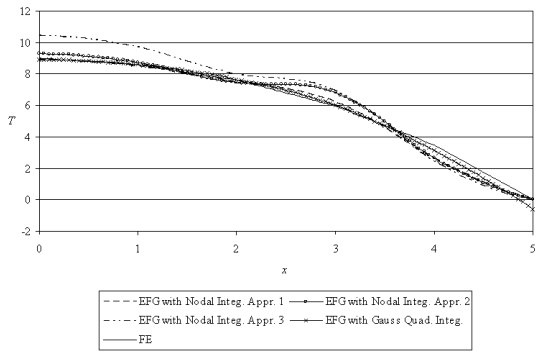

(a)

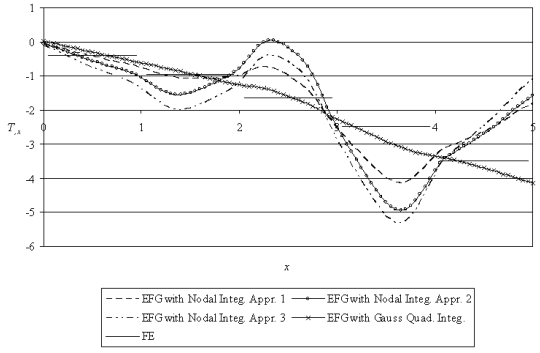

(b)

Figure 9. Analysis results of the square fin at $y = 0$ using FE and EFG methods with different methods of integration: (a) temperature (b) temperature derivative.

Strip Fin

A 6.0×5.0 strip fin subjected to an internal heat source:

$$Q(x, y) = 2\,\mathrm{sech}^2(x - 3)\tanh(x - 3) \tag{65}$$

With the boundary condition given by

$$\begin{aligned} &T(0, y) = -\tanh 3 \\ &T(6, y) = \tanh 3 \\ &T_{,x}(x, 0) = 0 \\ &T_{,x}(x, 0.5) = 0 \end{aligned} \tag{66}$$

is considered and modelled as shown in Figure 10.

Table 2. EFG errors and required assembling CPU time of analysis of the square fin using different numbers of Gauss points (based on a PIV 3.0 GHz processor).

n_G	Assembling CPU Time	Total Number of Gauss Points	$err(T)$
1	14sec	65	542.13%
2	42sec	140	17.76%
3	109sec	265	5.63%
4	172sec	440	3.20%
5	288sec	665	5.60%
6	426sec	940	20.88%
10	1058sec	2540	9.93%

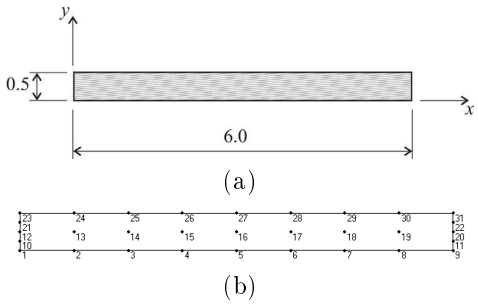

Figure 10. Analysis of the strip fin: (a) geometry (b) nodal arrangement.

The exact solution is:

$$T^{\text{ex}}(x,y) = \tanh(x-3) \tag{67}$$

The quadratic basis ($m = 6$) with the scaling factor $\alpha_\rho = 1.5$ and minimum radius of influence domain $\rho_{min} = 1.75$ is employed in the analysis. Gauss quadrature integration is performed using 8×1 cells, each including 4×4 Gauss points within the system domain and 2 Gauss points on any boundary segment. Table 4 compares assembling CPU time and relative errors for different integration rules. Numerical results for T and $T_{,x}$, and relative errors are illustrated in Figures (11)-(12), respectively. Figure 11 depicts the analysis results for both the temperature and its derivative at $y = 0.25$ using FE and EFG methods with different techniques of integration, while Figure 12 shows the relative error associated with the mentioned results in the same section. The proposed nodal integration technique, though has a lower level of accuracy, yet it is less expensive than the Gauss integration rule, and provides better results among the existing nodal integration approaches.

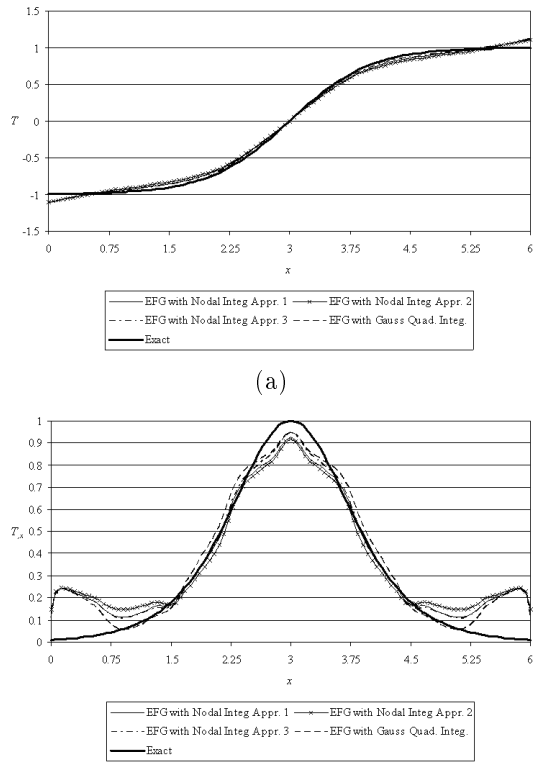

Figure 11. Analysis results of the strip fin at $y = 0.25$ using FE and EFG methods with different techniques of integration: (a) temperature (b) temperature derivative.

CONCLUSION

The element-free Galerkin method together with several numerical integration approaches categorised as Gauss quadrature and nodal integration rules have been successfully developed, and implemented for two-

Table 3. EFG errors and required assembling CPU time of analysis of the square fin using different types of integration (based on a PIV 3.0 GHz processor).

Integration Method	Assembling CPU Time	$err(T)$	$\sum_{J=1}^{N} A_J \Big/ A(\Omega)$	$cond(\mathbf{K}^*)$
EFG – Gauss Integ.	172sec	3.20%	——	1.044
EFG – Nodal Integ. Appr. 1	8sec	5.49%	14.703	1.000
EFG – Nodal Integ. Appr. 2	8sec	7.44%	12.292	1.000
EFG – Nodal Integ. Appr. 3	8sec	14.10%	2.003	1.000

Table 4. EFG errors and required assembling CPU time of analysis of the strip fin using different types of integration (based on a PIV 3.0 GHz processor).

Integration Method	Assembling CPU Time	$err(T)$	$err(T_{,x})$	$\sum_{J=1}^{N} A_J \Big/ A(\Omega)$	$cond(\mathbf{K}^*)$
EFG – Gauss Integ.	48sec	0.172%	3.819%	——	0.988
EFG – Nodal Integ. Appr. 1	12sec	0.307%	4.619%	57.727	0.998
EFG – Nodal Integ. Appr. 2	12sec	0.484%	5.659%	13.801	0.994
EFG – Nodal Integ. Appr. 3	12sec	0.248%	4.242%	6.401	0.959

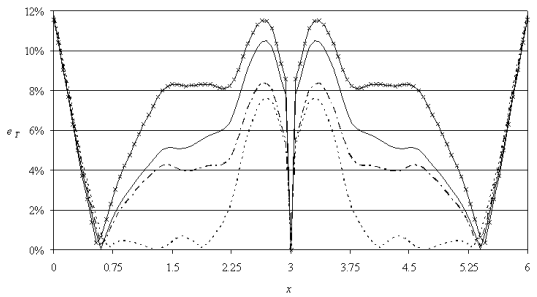

(a)

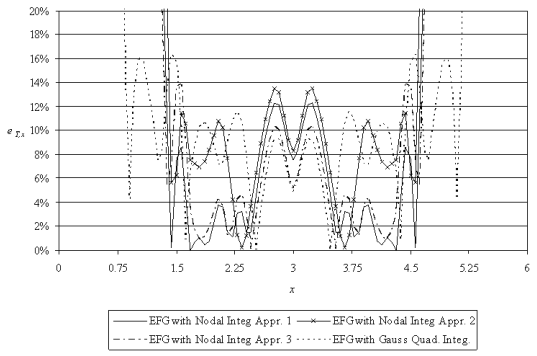

(b)

Figure 12. Relative error at $y = 0.25$ of the strip fin comparing different techniques of integration for: (a) temperature (b) temperature derivative.

dimensional analysis of steady-state heat transfer. Lagrange multipliers have been employed to enforce essential boundary conditions. Several numerical examples have been investigated to evaluate the efficiency and accuracy of the proposed approaches. Nodal integration techniques are much faster than the Gauss quadrature integration rule although they usually provide a lower level of accuracy. The nodal integration approaches presented in this article are expected to perform well for other similar applications such as transient heat transfer problems or general quasi-harmonic partial differential equations, and even lead to much faster results for three-dimensional problems with a proper level of accuracy.

Although very fast CPUs are nowadays available, the saved time using faster analytical approaches can be used for more important tasks in more complicated problems such as three-dimensional error estimation and adaptive analysis of transient heat transfer.

ACKNOWLEDGEMENTS

The authors would like to acknowledge the support received from the 'University of Tehran, Vice Chancellor for Research' under the grant number 614/2/988.

REFERENCES

1. Monaghan J.J., "Smoothed Particle Hydrodynamics", *Annu. Rev. Astron. Astrophys.*, **30**, PP 543-574(1972).
2. Belytschko T., Lu Y.Y. and Gu L., "Element-Free Galerkin Method", *Int. J. Numer. Meth. Eng.*, **37**, PP 229-256(1994).
3. Lu Y.Y., Belytschko T. and Gu L., "A New Implementation of the Element-Free Galerkin Method", *Comput. Meth. Appl. Mech. Eng.*, **113**, PP 397-414(1994).
4. Belytschko T., Krongauz Y., Organ D., Fleming M. and Krysl P., "Meshless Methods: An Overview and Recent Developments", *Comput. Meth. Appl. Mech. Eng.*, **139**, PP 3-47(1996).
5. Dolbow J. and Belytschko T., "An Introduction to Programming the Meshless Element-Free Galerkin Method", *Arch. Comput. Mech.*, **5**, PP 207-241(1998).
6. Atluri S.N. and Zhu T., "A New Meshless Local Petrov-Galerkin (MLPG) Approach in Computational Mechanics", *Comput. Mech.*, **22**, PP 117-127(1998).
7. Liu W.K., Jun S. and Zhang Y.F., "Reproducing Kernel Particle Methods", *Int. J. Numer. Meth. Eng.*, **20**, PP 1081-1106(1995).
8. Krysl P. and Belytschko T., "Analysis of Thin Plates by Element-Free Galerkin Method", *Comput. Mech.*, **17**, PP 26-35(1996).
9. Krysl P. and Belytschko T., "Analysis of Thin Shells by Element-Free Galerkin Method", *Int. J. Solids Struct.*, **33**, PP 3057-3080(1996).
10. Lu Y.Y., Belytschko T. and Tabbara M., "Element-Free Galerkin Methods for Wave Propagation and Dynamic Fracture", *Comput. Meth. Appl. Mech. Eng.*, **126**, PP 131-153(1995).
11. Belytschko T. and Fleming M., "Smoothing, Enrichment and Contact in the Element-Free Galerkin Method", *Computers and Structures*, **71**, PP 173-195(1999).
12. Singh I.V., Sandeep K. and Prakash R., "The Element Free Galerkin Method in Three Dimensional Steady State Heat Conduction", *Int. J. Computational Engineering Science*, **3**, PP 291-303(2002).
13. Singh I.V., Sandeep K. and Prakash R., "Heat Transfer Analysis of Two-Dimensional Fins Using A Meshless Element Free Galerkin Method", *Numerical Heat Transfer, Part A: Applications*, **44**, PP 73-84(2003).
14. Singh I.V., "Parallel Implementation of the EFG Method for Heat Transfer and Fluid Flow Problems", *Computational Mechanics*, **34**, PP 453-463(2004).
15. Singh I.V., "Meshless EFG Method in Three-Dimensional Heat Transfer Problems: a Numerical Comparison, Cost and Error Analysis", *Numerical Heat Transfer, Part A: Applications*, **45**, PP 199-220(2004).
16. Forouzan-sepehr S. and Mohammadi S., "Meshless Methods for the Analysis of Engineering Problems", *Research Report No. 614/2/988*, University of Tehran, (2004).

17. Lancaster P. and Salkauskas K., "Surfaces Generated by Moving Least Squares Methods", *Math Comput.*, **37**, PP 141-158(1981).
18. Zienkiewicz O.C. and Taylor R.L., *The Finite Element Method, vol. 1: The Basis*, Butterworth-Heinemann, Oxford, UK, PP 219-221(2002).
19. Duflot M. and Nguyen-Dang H., "A Truly Meshless Galerkin Method Based on A Moving Least Squares Quadrature", *Communications in Numerical Methods in Engineering*, **18**, PP 441-449(2002).
20. Beissel S. and Belytschko T., "Nodal Integration of the Element-Free Galerkin Method", *Comput. Meth. Appl. Mech. Eng.*, **139**, PP 49-74(1996).
21. Forouzan-sepehr S., "UTELFree2D Technical Manual Version 1", University of Tehran, (2005).